Biosensors and Bioelectronics 167 (2020) 112481

Contents lists available at ScienceDirect

Biosensors and Bioelectronics

journal homepage: http://www.elsevier.com/locate/bios

In-situ synthesis of 3D Cu_2O@Cu-based MOF nanobelt arrays with improved conductivity for sensitive photoelectrochemical detection of vascular endothelial growth factor 165

Weisu Kong, Mei-Hao Xiang, Lian Xia, Mengying Zhang, Rong-Mei Kong **, Fengli Qu *

College of Chemistry and Chemical Engineering, Qufu Normal University, Qufu Shandong, 273165, PR China

ARTICLE INFO

Keywords:
Photoelectrochemical
Rolling circle amplification
Vascular endothelial growth factor 165
Semiconductor@MOF

ABSTRACT

Construction of novel photoelectrochemical (PEC) materials with unique structures can effectively improve the photoelectric conversion efficiency. Here, a self-supported Cu_2O@Cu-MOF/copper mesh (CM) nanobelt arrays with high specific surface area, high orientation, and high photoelectric conversion performance is obtained by in-situ grown strategy. Such PEC aptasensor is constructed based on the Cu_2O@Cu-MOF/CM combined with rolling circle amplification and enzymatic biocatalytic precipitation for vascular endothelial growth factor 165 analysis. This strategy achieves excellent cooperative signal amplification, which greatly improves the detection sensitivity. The PEC aptasensor exhibited a wide calibration ranged from 10 to 1×10^8 fM with a detection limit down to 2.3 fM ($S/N = 3$). The construction of semiconductor@MOFs has developed the potential application of MOFs in photoelectrochemical and found a reliable path for ultrasensitive detection of biomarkers.

1. Introduction

In recent years, photoelectrochemical (PEC) has attracted extensive research as a promising analytical method (Hao et al., 2020; Xu et al., 2020). Compared with traditional electrochemistry, PEC possesses advantages of high sensitivity, great selectivity and low-cost determination due to the separation of the excitation light source and the output signal (Kong et al., 2020a; Sun et al., 2019; Liu et al., 2019; Zhu et al., 2019). More importantly, photoactive materials are critical for constructing PEC biosensing platforms with excellent analytical performance. The development of high-performance PEC materials is usually limited by the problems of unstable photocurrent and low electronic conversion efficiency. Therefore, in order to obtain more stable photoelectric conversion efficiency, it is necessary to develop new nanomaterials with larger contact area and strong stability under an excitation source to improve the electron transfer rate.

Metal organic frameworks (MOFs) are composed of metal ions/clusters and bridged ligands through coordination bonds with greater porosity and specific surface area (Liu et al., 2020; Wu et al., 2019; Zhao et al., 2018). Ligands in MOFs can absorb light energy, and photoelectrons can be further injected into the metal oxygen cluster through the charge transfer from the ligand to the cluster to generate electron-hole pairs, showing extraordinary semiconductor performance (Liu et al., 2018a; Li et al., 2019). However, the MOFs usually have disadvantages such as disordered orientation and low conductivity, which are not conducive to electron transfer (Cai et al., 2017; Deng et al., 2018). Therefore, there is an urgent need to develop new MOFs-based materials with high orientation and uniform interface structure to improve the photoactive performance.

Recently, MOFs-based materials have been widely reported for constructing of PEC biosensors. Liu's team established a PEC biosensor platform using PCN-224/rGO as the photoactive material for p-arsanilic acid detection (Peng et al., 2019). Yang's group constructed PEC sensor based on Au-NPs@Zn-MOF material to detect squamous cell carcinoma antigen (Wei et al., 2019). Actually, how to enhance the photoelectric conversion efficiency of MOFs is still the key problem for its development in the field of PEC bioanalysis. Three-dimensional (3D) nanomaterials can promote electron transfer and improve electrical conductivity due to their large specific surface area, uniform interface structure and high orientation (Guo et al., 2019; Kong et al., 2020b). More importantly, the heterostructure formed by combining 3D MOFs with other semiconductor materials shows better PEC performance due

* Corresponding author.
** Corresponding author.
E-mail addresses: kongrongmei@126.com (R.-M. Kong), fengliquhn@hotmail.com (F. Qu).

https://doi.org/10.1016/j.bios.2020.112481
Received 31 May 2020; Received in revised form 8 July 2020; Accepted 27 July 2020
Available online 3 August 2020

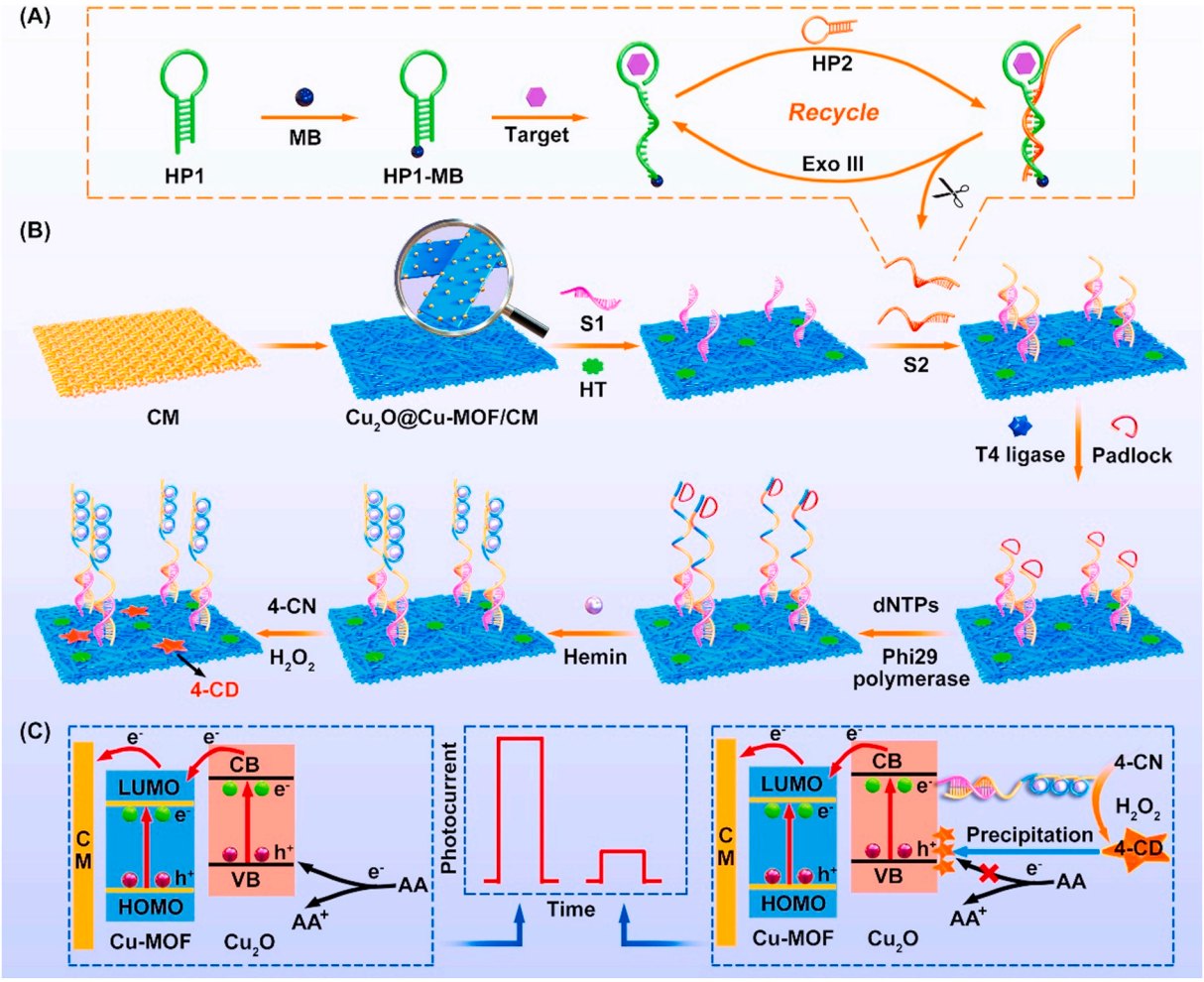

Scheme 1. Schematic diagrams of (A) Exo III-assisted target cycle amplification strategy; (B) preparation process of RCA based PEC aptasensor; (C) mechanism on the charge-carrier transfer of Cu_2O@Cu-MOF/CM.

to band matching (Li et al., 2018a; Song et al., 2019; Zhan et al., 2013). For example, some metal oxides (TiO_2, ZnO, Fe_3O_4, Cu_2O) show excellent semiconductor performance in PEC applications (Li et al., 2018a; Wang et al., 2008; Zhang et al., 2018a). Therefore, we reasonably believe that the successful preparation of 3D metal oxide@MOFs nanoarray structures can effectively improve the photoelectric conversion efficiency.

In this paper, the $Cu(OH)_2$ nanowire arrays (NWAs) grown on copper mesh (CM) by in-situ oxidation reaction are prepared and further used as a precursor to prepare Cu_2O@Cu-MOF/CM nanocomposites successfully (Cao et al., 2019). The as-prepared 3D nanoarray materials have large specific surface area and excellent stability, which is favorable to improve the performance of PEC. On this basis, we propose a novel PEC aptasensor for ultrasensitive detection of vascular endothelial growth factor 165 ($VEGF_{165}$; Scheme 1), considering that the expression of $VEGF_{165}$ in vascular tissues plays a prominent role in normal and pathological angiogenesis (Da et al., 2018; Fu et al., 2020). Specifically, the captured DNA (S1) is modified on the surface of the Cu_2O@Cu--MOF/CM electrode by Cu–S bond (Pakiari and Jamshidi, 2010). In the exonuclease III (Exo III)-assisted recycling strategy (Scheme 1A), the $VEGF_{165}$ is introduced to obtain a large amount of single-stranded DNA (S2) which can be complementary hybridized with S1. In the presence of padlock probe, which can be hybridized with the tail sequence of S2, and the presence of T4 DNA ligase, phi29 polymerase and deoxyribonucleoside 5′-triphosphate (dNTPs) mixture, the rolling circle amplification (RCA) reaction is triggered. The resulting large amount of duplicate G-rich DNA sequences can specifically bind with hemin to form stable G-quadruplex structures with the function of DNAzyme. The DNAzyme can catalyze the bioprecipitation reaction of 4-chloro-1-naphthol (4-CN) to reduce the PEC signal, thus can be employed for the detection of $VEGF_{165}$ (Scheme 1B). The successfully construction of the aptasensor not only provides a new path for sensitive determination of targets, but also extends the application of MOFs in the field of PEC sensing.

2. Experimental section

2.1. In-situ growth of Cu_2O@Cu-MOF NBAs on copper mesh

CM treatment: ultrasound with dilute hydrochloric acid for 1 min, followed by sonicating with deionized water 2–3 times. Firstly, 3.2 g of NaOH and 0.91 g of $(NH_4)_2S_2O_8$ were dissolved in 20 mL of water, respectively. Subsequently, the $(NH_4)_2S_2O_8$ solution was poured into the NaOH solution, and the treated CM was put into the mixed solution for 20 min. The CM was taken out and washed with water and ethanol to obtain a dark blue $Cu(OH)_2$ precursor.

Cu_2O@Cu-MOF/CM were prepared by the above $Cu(OH)_2$/CM as precursor using a typical hydrothermal method (Yang et al., 2019). Specifically, 0.5815 g $C_8H_6O_4$ and 1.1416 g $Cu(NO_3)_2{\cdot}3H_2O$ were dispersed in 70 mL of DMF. Then, 5 mL C_2H_5OH and 5 mL H_2O were added, and stirred continuously for 10 min at room temperature. The above-mentioned $Cu(OH)_2$ precursor and the mixed solution were

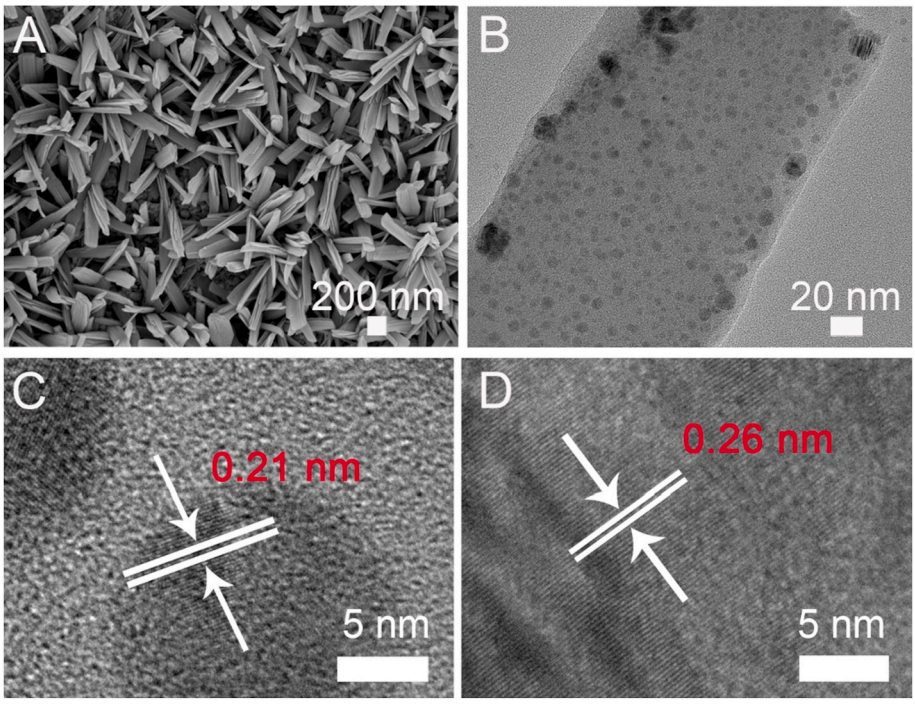

Fig. 1. SEM (A) and TEM image (B) of Cu_2O@Cu-MOF. HRTEM image for Cu_2O@Cu-MOF; (C) the lattice fringe of Cu_2O; (D) the lattice fringe of Cu-MOF.

transferred to a 100 mL Teflon-lined autoclave, and maintained at 120 °C for 12 h. The obtained Cu_2O@Cu-MOF/CM were washed with water and ethanol, and dried at 60 °C.

2.2. Exonuclease III-aided target recycling

As shown in Scheme 1A, magnetic beads (MB; 50 μL) and activator (50 μL, 20 mM EDC and 10 mM NHS) were mixed for 2 h to activate the carboxyl group of MB. The supernatant was removed by magnetic separation, and the activated MB was dispersed in 50 μL of ultrapure water. Subsequently, aminated aptamers (HP1, 50 μL, 4 μM) were mixed with activated MB overnight, and aptamers were ligated to MB via acylation reaction. Different concentrations of targets ($VEGF_{165}$; 50 μL) and HP2 (50 μL, 4 μM) were incubated with the above HP1-MB at 37 °C for 2 h. The HP1 can specifically capture $VEGF_{165}$ to open the hairpin structure, and the naked DNA sequence can hybridize with HP2. Subsequently, the Exonuclease III (Exo III, final concentration of 2 $U{\cdot}\mu L^{-1}$) was added to trigger the cycle amplification reaction to obtain S2. Finally, S2 was separated by magnetic separation for the next assembly of the PEC sensor. The buffer used was Tris-HCl (pH 7.4).

2.3. Fabrication of the PEC biosensor

Firstly, S1 was treated with 10 mM Tris-HCl buffer (pH 7.4) containing 10 mM TCEP for 1 h at room temperature to reduce disulfide bonds. Afterward, 10 μL of S1 (2 μM) were immobilized on the surface of the Cu_2O@Cu-MOF/CM electrode by Cu–S bond and incubated overnight. Then, 10 μL of HT (0.1 mM) solution were added dropwise and incubated for 1 h to block non-specific sites. Next, 10 μL of S2 were modified on the electrode surface, and incubated for 2 h at 37 °C. After that, 10 μL of 2 μM padlock DNA were incubated at 37 °C for 1 h. Furthermore, 5 μL of 10 U T4 ligase and 5 μL of 10 × T4 ligase reaction buffer were added and hold for 2 h. Subsequently, 2 μL of 10 U phi29 polymerase, 5 μL of 10 × phi29 polymerase reaction buffer and 5 μL of 10 mM dNTPs were decorated on the obtained electrode surface for 2 h at 37 °C to achieve RCA. The RCA reaction produces a large number of G-rich DNA sequences. When hemin was added, it can form a stable G-quadruplex structure and had the function of DNAzyme. The obtained electrode (hemin/RCA/padlock/HT/S1/Cu_2O@Cu-MOF/CM) was incubated with 4-CN (1.0 mg mL^{-1}) and H_2O_2 (10 mM) solution for 10 min to perform a nanoenzyme-catalyzed precipitation reaction. The assembly process of PEC biosensor was shown in Scheme 1B.

3. Results and discussion

3.1. Morphology characterization of the Cu_2O@Cu-MOF nanobelt arrays

The morphology and structure of $Cu(OH)_2$ nanoarrays and Cu_2O@Cu-MOF composites were investigated by scanning electron microscopy (SEM) and transmission electron microscopy (TEM). As shown in Figs. S1A and S1B, the $Cu(OH)_2$ nanowire array is evenly distributed on the substrate surface. In addition, SEM image of Cu_2O@Cu-MOF/CM synthesized with $Cu(OH)_2$ NWAs as precursors shows a good alignment of the nanobelt arrays (Fig. 1A). TEM images (Fig. 1B) show that the nanobelts are successfully synthesized and Cu_2O nanoparticles are grown with nanobelts as templates. The large specific surface area of the composite material and the uniform distribution of Cu_2O are beneficial to shorten the electron transfer path and increase the electron-hole separation rate. Furthermore, the lattice fringes of 0.21 and 0.26 nm in the high-resolution TEM (HRTEM) images can be attributed to (200) crystal plane of Cu_2O (Fig. 1C) and (201) crystal plane of the Cu-MOF (Fig. 1D), respectively (Yang et al., 2019). Fig. S1 is the energy dispersive X-ray spectrometry (EDS) of Cu_2O@Cu-MOF, the elemental mapping verifies the existence and uniform distribution of Cu, C and O elements.

3.2. Compositional and spectroscopic characterization of Cu_2O@Cu-MOF nanobelt arrays

Fourier transform infrared (FT-IR) spectra and X-ray photoelectron spectroscopy (XPS) survey spectra were used to prove the functional group and elemental composition of the material, respectively. As shown in Fig. 2A, two peaks at 3610 and 3273 cm^{-1} in the FT-IR spectrum can be corresponded to the O–H stretching vibration, indicating the presence of coordinated water molecules (Arul et al., 2017). Fig. 2B is an enlarged view of Fig. 2A. The characteristic peaks at 1665

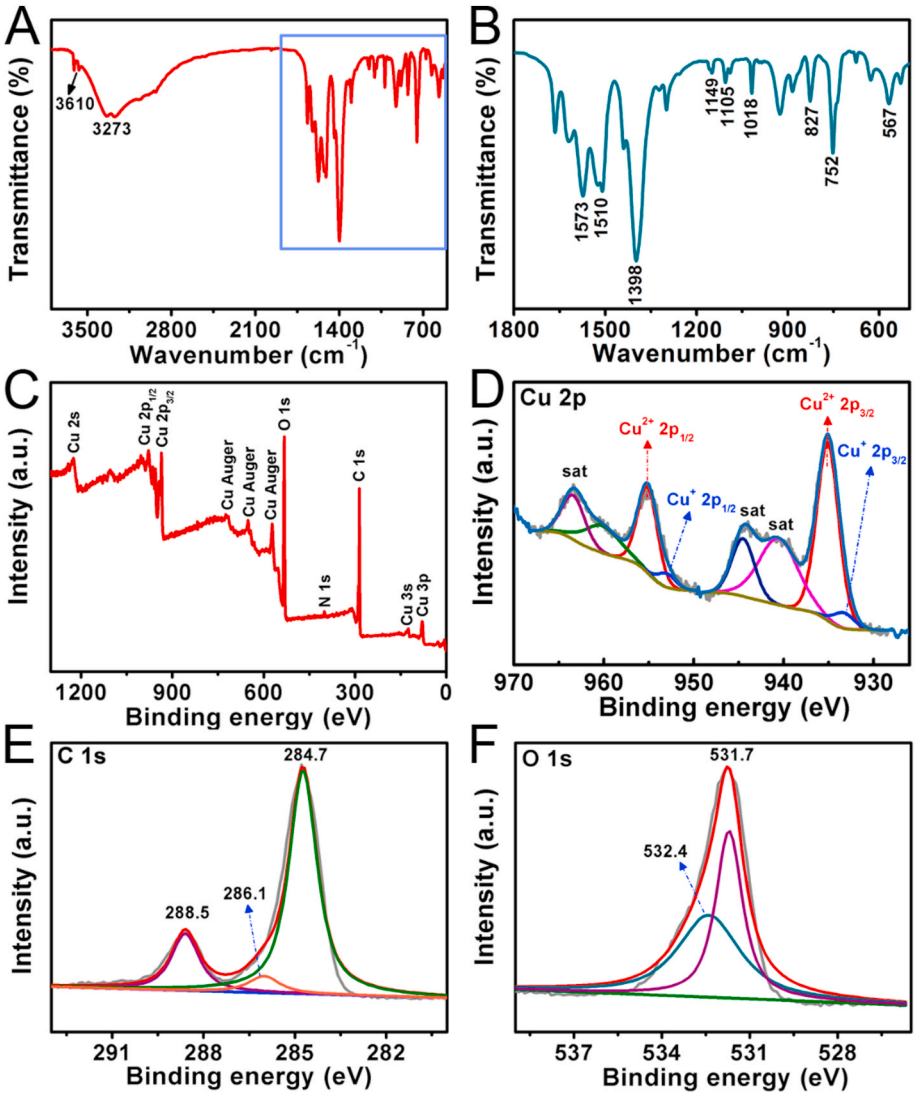

Fig. 2. (A and B) FT-IR spectra of Cu_2O@Cu-MOF (B is an enlarged view of the area labeled A); (C) XPS analysis of the full region of Cu_2O@Cu-MOF/CM; (D) high-resolution XPS spectra for Cu 2p; (E) C 1s and (F) O 1s of Cu_2O@Cu-MOF.

and 1398 cm^{-1} can be assigned to the asymmetric and symmetric stretching vibration of the coordination group (O═C–O). Meanwhile, the C–H stretching vibrations are attributed to the characteristic peaks of 1149, 1105, 1018, and 827 cm^{-1}, respectively. Furthermore, the two absorption bands at 752 and 567 cm^{-1} can be attributed to the Cu–O stretching vibration (Wang et al., 2015).

The XPS evaluates the compositions and valence states of elements in Cu_2O@Cu-MOF. The XPS spectrum in Fig. 2C indicates the presence of C, O, and Cu elements, which is consistent with the infrared results described above. In the Cu 2p region (Fig. 2D), the four peaks at 955.1, 935.1, 953.0 and 933.3 eV are corresponded to the Cu^{2+} $2p_{1/2}$, Cu^{2+} $2p_{3/2}$, Cu^{+} $2p_{1/2}$ and Cu^{+} $2p_{3/2}$ with four shakeup satellite peak (Sat.) at

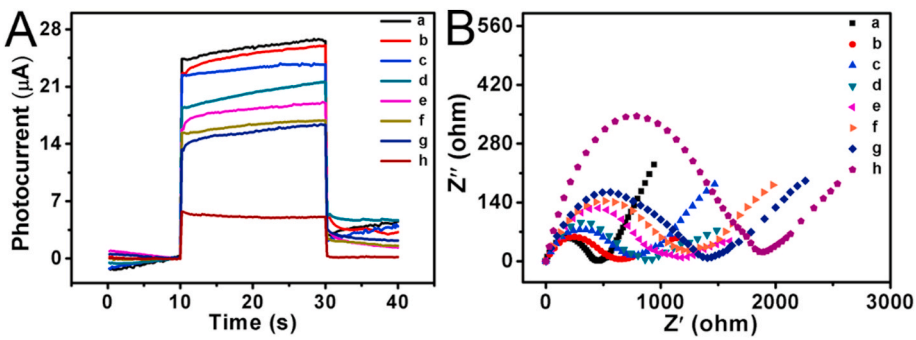

Fig. 3. (A) Photocurrent and (B) EIS responses of (a) Cu_2O@Cu-MOF/CM; (b) S1/Cu_2O@Cu-MOF/CM; (c) HT/S1/Cu_2O@Cu-MOF/CM; (d) S2/HT/S1/Cu_2O@Cu-MOF/CM; (e) Padlock/S2/HT/S1/Cu_2O@Cu-MOF/CM; (f) RCA/Padlock/S2/HT/S1/Cu_2O@Cu-MOF/CM; (g) Hemin/RCA/Padlock/S2/HT/S1/Cu_2O@Cu-MOF/CM; (h) Hemin/RCA/Padlock/S2/HT/S1/Cu_2O@Cu-MOF/CM followed by incubation with 4-CN and H_2O_2.

963.9, 960.1, 944.5 and 940.6 eV, respectively, indicating that the Cu element exists as Cu^{2+} (Deng et al., 2019). Moreover, the peaks of C 1s spectrum at 288.5, 286.1 and 284.7 eV are corresponded to O–C═O, C–O–C, C–C groups (Liu et al., 2018b; Zhang et al., 2018b), respectively (Fig. 2E). In Fig. 2F, the peaks of the O 1s spectrum at 532.4 and 531.7 eV can be attributed to C–O and H–O–C groups (Du et al., 2018). The above results indicate the successful preparation of highly oriented Cu_2O@Cu-MOF NBAs.

3.3. PEC and electrochemical impedance spectroscopy (EIS) characterizations of the PEC biosensor

PEC and EIS characterizations were used to investigate the stepwise fabrication process of electrodes. As shown in Fig. 3A, the PEC characterization is performed in a phosphate buffer saline (PBS, 0.1 M, pH 7.4) containing ascorbic acid (AA, 0.1 M). As displayed by curve a, a significant photocurrent is observed due to the strong electrical conductivity of Cu_2O@Cu-MOF/CM. The continuous assembly of S1 (curve b), hexanethiol (HT, curve c) and S2 (curve d) results in a gradual decrease of the photocurrent responses, which may be due to poor charge transport of the DNA skeletons and organic small molecules (Li et al., 2018b; Ye et al., 2017; Zhang et al., 2019). Subsequently, the modification of padlock probe and T4 ligase on the electrode surface resulted in the further reduction of photocurrent response (curve e). With the introduction of phi29 polymerase and deoxyribonucleoside triphosphate (dNTPs), the photocurrent response is observed to decrease again (curve f), because a large amount of G-rich DNA sequences produced by the RCA reaction hinder the electron transfer. The above G-rich sequences can specifically bind with hemin to form stable G-quadruplex structures with DNAzyme function, resulting in a slight decrease in photocurrent (curve g). When 4-CN and H_2O_2 are added, the DNAzyme can catalyze the bioprecipitation of 4-CN to generate benzo-4-chloro-hexadienone (4-CD), resulting in the greatly reduced photocurrent response (curve h). This is mainly due to the 4-CD resulted efficient inhibition of electron transfer and increase in steric hindrance.

Scheme 1C illustrates the possible electron transfer mechanism of Cu_2O@Cu-MOF/CM photoactive materials. Under the light irradiation of 523 nm, the electrons of Cu_2O transfer from the valence band (VB) to the conduction band (CB). The electrons in the CB of the Cu_2O transfer to the lowest unoccupied molecular orbital (LUMO) of Cu-MOF due to the energy band matching. At the same time, the electrons of Cu-MOF jump from the highest occupied molecular orbital (HOMO) to LUMO under the irradiation of light, and then transfer to CM. Furthermore, the AA in the electrolyte is acted as electron donors and used to clear holes, which can hinder the recombination of electron-hole, and enhance the photocurrent response. In the presence of target, the Exo III-assisted recycling amplification is performed (Scheme 1A), and the resulting single-stranded DNA (S2) can be used for PEC sensor assembly. In combination of Scheme 1A with Scheme 1B, the RCA reaction is triggered to produce stable G-quadruplex structures with DNAzyme activity that can be used to catalyze 4-CN to generate insoluble precipitate 4-CD, thus preventing AA from providing electrons and reducing the photocurrent signal.

The stepwise electrode modification process was characterized by EIS in $[Fe(CN)_6]^{3-/4-}$ buffer (5 mM). In EIS measurements, the semicircle diameters at high frequency region is equal to the electron transfer resistance (R_{et}), the smaller the diameter of the semicircle, the stronger the electron transport capacity. There is a small semicircle for Cu_2O@Cu-MOF/CM due to its large specific surface area thus excellent electron transfer capability (Fig. 3B, curve a). When S1 (curve b), HT (curve c) and S2 (curve d) are immobilized on the electrode, the R_{et} slightly increases because of the low conductivity of DNA phosphate skeleton. A further increase of the R_{et} is found after incubating with padlock probe (curve e). The RCA reaction after adding phi29 polymerase and dNTPs further increases the R_{et} because of the long-chain amplification products increased steric hindrance effect (curve f).

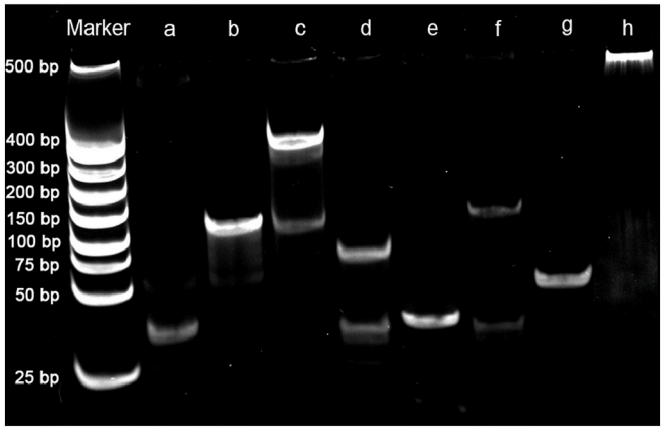

Fig. 4. PAGE analysis: (a) HP1; (b) HP2; (c) HP1+HP2 (d) S2; (e) S1; (f) S1+S2; (g) padlock; (h) RCA product.

After the specific binding of hemin by the G-rich RCA products to form G-quadruplexes, a slight increase of R_{et} is observed (curve g). When 4-CN and H_2O_2 are added, the G-quadruplex can act as DNAzyme to catalyze the production of bioprecipitation which can hinder the electron transfer effectively, thereby increasing the R_{et} significantly (curve h). The stepwise EIS characterization results prove that the aptasensor has been successfully prepared.

3.4. Polyacrylamide-gel-electrophoresis (PAGE) characterization of DNA reaction

The RCA strategy was employed to produce large number of repeated G-rich sequences to realize the PEC signal amplification. Therefore, the successful execution of the RCA reaction was verified by PAGE, and the results were presented in Fig. 4. The bands of lanes a, b, e and g correspond to HP1, HP2, S1 and padlock probe, respectively. When the target is present, the mixture of HP1 and HP2 appears a slowly migrating strong band (lane c), indicating the successful hybridization of HP1 and HP2. This can be attributed to the fact that the specific binding of $VEGF_{165}$ by the aptamer sequence in HP1 results in the open of the hairpin structure, and the exposed free sequence can act as a catalyst to trigger the catalyzed hairpin assembly and thus open the HP2 hairpin structure. Compared to lane c, lane d has a significantly faster band shift, which is due to the successful implementation of the Exo III enzyme-assisted target cycle amplification strategy. Furthermore, lane f observes slower electrophoretic mobility bands than lanes a and e, indicating the successful hybridization of S1 and S2. As expected, a distinct new band appears at the beginning of lane h, confirming that the high molecular weight RCA products are successfully formed.

3.5. Analytical performance of the biosensor

Quantitative applications of PEC biosensors were evaluated using different concentrations of $VEGF_{165}$ under optimal conditions (seen Supporting Information). According to the results shown in Fig. 5A, the PEC signal gradually decreases with the increase of $VEGF_{165}$ concentration (10–1 × 10^8 fM). As shown in Fig. 5B, the photocurrent response and the logarithm of $VEGF_{165}$ concentration show a favorable linear relationship. The linear equation is $A = 16.24–1.79\ \lg C_{VEGF165}$ (fM) with the correlation coefficient of $R^2 = 0.9900$, and the detection limit is estimated down to 2.3 fM ($S/N = 3$). As shown in Table S2, compared with the reported biosensors, the proposed sensing platform achieves a superior sensitivity for the detection of $VEGF_{165}$. This is attributed to the effective combination of various signal amplification strategies resulted excellent synergistic signal amplification, which leads to the production of a large number of DNAzymes to promote the bioprecipitation, thus

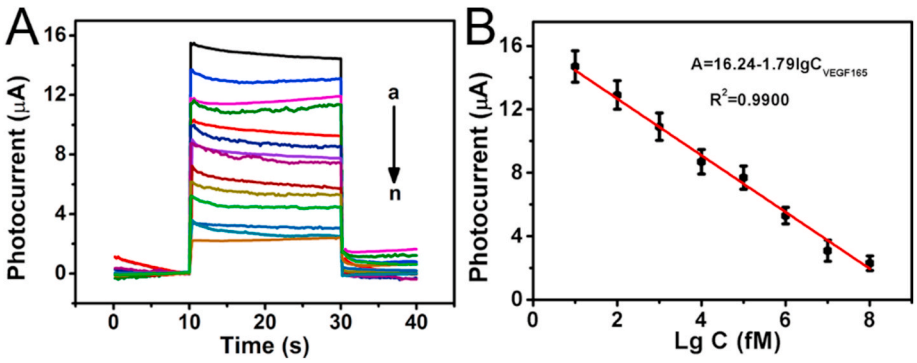

Fig. 5. (A) Photocurrent responses of the different concentration of $VEGF_{165}$, from a to h: 10, 100, 500, 1×10^3, 5×10^3, 1×10^4, 5×10^4, 1×10^5, 5×10^5, 1×10^6, 5×10^6, 1×10^7, 5×10^7 and 1×10^8 fM, respectively; (B) the calibration plot between the photocurrent and the logarithm of $VEGF_{165}$ concentration. Error bars: the standard deviation of the three measurements.

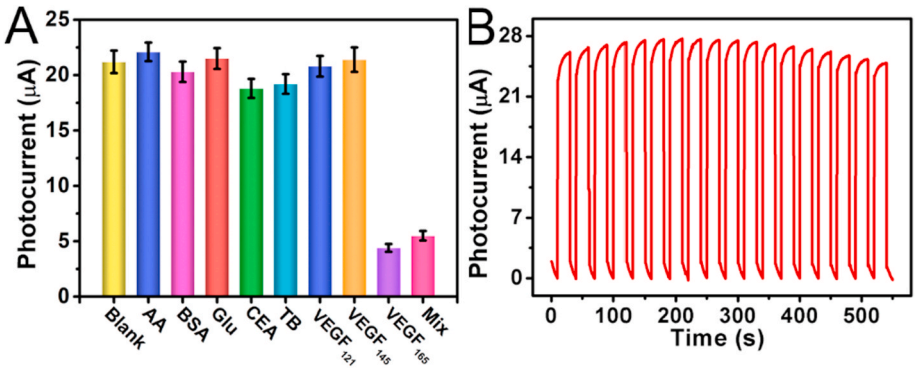

Fig. 6. (A) The selectivity of the $VEGF_{165}$-sensing platform. The concentration of $VEGF_{165}$ was 1 nM, and the concentrations of other interferences were 10 nM; (B) stability of the Cu_2O@Cu-MOF/CM. Error bars: the standard deviation of the three measurements.

significantly reducing the background signal.

Under the same experiment conditions, some interferences were incubated to test the specificity of the aptasensor. As depicted in Fig. 6A, using AA, bovine serum albumin (BSA), glucose (Glu), carcinoembryonic antigen (CEA), thrombin (TB), $VEGF_{121}$ and $VEGF_{145}$ (concentration of 10 nM) to replace the target, only weak photocurrent changes can be observed compared to the blank signal. However, when $VEGF_{165}$ is introduced (concentration of 1 nM), the photocurrent signal decreases significantly. In addition, the mixture of $VEGF_{165}$ and the other interferences could also induce significant photocurrent signal decrease as same as the presence of $VEGF_{165}$ alone, indicating the satisfactory selectivity of the biosensor for $VEGF_{165}$. In addition, excellent stability of PEC electrode is the key of extending the potential application of PEC sensor in the sensing field. Under the optimal conditions, the stability of PEC materials was tested using continuous lighting "on-off". As can be seen from Fig. 6B, after 560 s of detection, there is no significant change in photocurrent. The experimental results suggested that the constructed PEC electrode has superior stability.

3.6. Practical analysis in serum samples

In order to evaluate the potential application of the biosensor in clinical diagnosis, a test method for recovery of $VEGF_{165}$ in human serum was designed. Serum was provided by the Qufu Normal University School Hospital. A standard addition method and relative standard deviation (RSD) were used for the average recovery test. Specifically, dilute serum 100-fold with PBS buffer (pH 7.4), and then add targets with different concentrations (0.5, 10, 100, 500, 1000, 5000 and 10000 pM) for PEC detection. As shown in Table S3, the recovery rate of $VEGF_{165}$ is 95.6–105.6%, and the RSD is 1.6%–2.7%, indicating that the biosensor is satisfactory for quantitative analysis in biological samples.

4. Conclusion

In this work, using $Cu(OH)_2$ as a precursor, a novel 3D nanobelt array structure Cu_2O@Cu-MOF/CM have been successfully prepared by in-situ growth method. The material characterization experiments suggested that the synthesized Cu_2O@Cu-MOF/CM NBAs have excellent PEC properties. Taking the above nanoarray material as the PEC electrode and combining with RCA and enzymatic biocatalytic precipitation strategies, an ultrasensitive PEC aptasensor for $VEGF_{165}$ was constructed. Furthermore, the selectivity and stability of the sensing platform were also well verified. This work not only successfully developed the application of semiconductor@MOFs array structure in the field of PEC bioanalysis, but also offered a novel perspective for the development of other 3D MOFs structures in PEC sensors.

Declaration of competing interest

The authors declare that they have no known competing financial interests or personal relationships that could have appeared to influence the work reported in this paper.

Acknowledgements

This work was supported by the National Natural Science Foundation of China (21775089), Outstanding Youth Foundation of Shandong Province (ZR2017JL010), Taishan Scholars Program of Shandong Province (tsqn201909106), and the Key Research and Development Program of Jining City (2018ZDGH032).

Appendix A. Supplementary data

Supplementary data to this article can be found online at https://doi.org/10.1016/j.bios.2020.112481.

References

Arul, P., Abraham John, S., Electroanal, J., 2017. Chem 799, 61–69.
Cai, G., Zhang, W., Jiao, L., Yu, S., Jiang, H., 2017. Chem 2, 791–802.
Cao, X.Y., Cui, L., Liu, B.P., Liu, Y., Jia, D.D., Yang, W.R., Razal, J.M., Liu, J.Q., 2019. J. Mater. Chem. A 7, 3815–3827.
Deng, T., Lu, Y., Zhang, W., Sui, M., Shi, X., Wang, D., Zheng, W., 2018. Adv. Energy Mater. 8, 1702294.
Da, H.M., Liu, H.Y., Zheng, Y.N., Yuan, R., Chai, Y.Q., 2018. Biosens. Bioelectron. 101, 213–218.
Deng, X., Li, R., Wu, S., Wang, L., Hu, J., Ma, J., Jiang, W., Zhang, N., Zheng, X., Gao, C., Wang, L., Zhang, Q., Zhu, J., Xiong, Y., 2019. J. Am. Chem. Soc. 141, 10924–10929.
Du, H.T., Guo, X.X., Kong, R.M., Qu, F.L., 2018. Chem. Commun. 54, 12848–12851.
Fu, Y.M., Zou, K., Liu, M.Y., Zhang, X.H., Du, C.C., Chen, J.H., 2020. Anal. Chem. 92 (1), 1189–1196.
Guo, X.X., Liu, S.P., Yang, M.H., Du, H.T., Qu, F.L., 2019. Biosens. Bioelectron. 139, 111312–111317.
Hao, N., Dai, Z., Xiong, M., Hua, R., Lu, J.W., Wang, K., 2020. Sens. Actuat. B-Chem. 306, 127594.
Kong, W.S., Guo, X.X., Jing, M., Qu, F.L., Lu, L.M., 2020a. Biosens. Bioelectron. 150, 111875–111881.
Kong, W.S., Qu, F.L., Lu, L.M., 2020b. Anal. Bioanal. Chem. 412, 841–848.
Liu, M.C., Ke, H.Y., Sun, C.Q., Wang, G.Q., Wang, Y., Zhao, G.H., 2019. Talanta 194, 266–272.
Liu, J., Yang, G.P., Jin, J., Wu, D., Ma, L.F., Wang, Y.Y., 2020. Chem. Commun. 56, 2395–2398.
Liu, H., Xu, C.Y., Li, D.D., Jiang, H.L., 2018a. Angew. Chem. Int. Ed. 57, 5379–5383.
Li, M.J., Wang, H.J., Yuan, R., Chai, Y.Q., 2019. Chem. Commun. 55, 10772–10775.
Li, X., Liu, S., Fan, K., Liu, Z., Song, B., Yu, J., 2018a. Adv. Energy Mater. 8, 1800101.
Liu, Q., Xie, L., Shi, X., Du, G., Asiri, A., Luo, Y., Sun, X., 2018b. Inorg. Chem. Front. 5 (7), 1570–1574.
Li, M.J., Xiong, C., Zheng, Y.N., Liang, W.B., Yuan, R., Chai, Y.Q., 2018b. Anal. Chem. 90 (13), 8211–8216.
Peng, M., Guan, G.J., Deng, H., Han, B., Tian, C., Zhuang, J.Y., Xu, Y.Y., Liu, W.Z., Lin, Z., 2019. Environ. Sci-Nano 6, 207–215.
Pakiari, A.H., Jamshidi, Z., 2010. J. Phys. Chem. A 114, 9212–9221.
Sun, C.Q., Liu, M.C., Sun, H.H., Lu, H.X., Zhao, G.H., 2019. Biosens. Bioelectron. 140, 111352.
Song, H.H., Sun, Z.Q., Xu, Y., Han, Y.D., Xu, J.L., Wu, J.B., Sun, T., Meng, H., Zhang, X., 2019. Separ. Purif. Technol. 228, 115764–115774.
Wu, Y.P., Tian, J.W., Liu, S., Li, B., Zhao, J., Ma, L.F., Li, D.S., Lan, Y.Q., Bu, X.H., 2019. Angew. Chem. Int. Ed. 58, 12185–12189.
Wei, Q.X., Wang, C., Zhou, X., Wu, T., Wang, Y.Y., Li, C.Y., Yang, N.J., 2019. Biosens. Bioelectron. 142, 111540–111548.
Wang, G., Chen, D., Zhang, H., Zhang, J., Li, J., 2008. J. Phys. Chem. C 112, 8850–8855.
Wang, X., Lu, X.B., Wu, L.D., Chen, J.P., 2015. Biosens. Bioelectron. 65, 295–301.
Xu, L., Duan, W., Chen, F., Zhang, J.M., Li, H.N., 2020. J. Hazard Mater. 400, 123162.
Yang, L., Zhu, G.L., Wen, H., Guan, X., Sun, X., Feng, H., Tian, W.L., Zheng, D.C., Cheng, X.W., Yao, Y.D., 2019. J. Mater. Chem. A 7, 8771–8776.
Ye, C., Wang, M.Q., Luo, H.Q., Li, N.B., 2017. Anal. Chem. 89, 11697–11702.
Zhu, Y.C., Xu, Y.T., Xue, Y., Fan, G.C., Zhang, P.K., Zhao, W.W., Xu, J.J., Chen, H.Y., 2019. Anal. Chem. 91, 6419–6423.
Zhao, Y., Wang, L., Fan, N.N., Han, M.L., Yang, G.P., Ma, L.F., 2018. Cryst. Growth Des. 18 (11), 7114–7121.
Zhan, W.W., Kuang, Q., Zhou, J.Z., Kong, X.J., Xie, Z.X., Zheng, L.S., 2013. J. Am. Chem. Soc. 135, 1926–1933.
Zhang, Q., Wang, H.Y., Dong, Y.X., Yan, J.T., Ke, X.B., Wu, Q.P., Xue, S., 2018a. Sol. Energy 171, 388–396.
Zhang, X.X., Liu, Q., Shi, X.F., Asiri, A.M., Sun, X.P., 2018b. Inorg. Chem. Front. 5, 1405–1408.
Zhang, L., Shi, X.M., Xu, Y.T., Fan, G.C., Yu, X.D., Liang, Y.Y., Zhao, W.W., 2019. Biosens. Bioelectron. 134, 103–108.